Monthly Notices
of the
ROYAL ASTRONOMICAL SOCIETY

MNRAS **467,** 1300–1312 (2017) doi:10.1093/mnras/stx180
Advance Access publication 2017 January 22

# Molecular cloud photoevaporation and far-infrared line emission

L. Vallini,[1,2,3★] A. Ferrara,[4,5] A. Pallottini[4,6,7] and S. Gallerani[4]

[1]*Nordita, KTH Royal Institute of Technology and Stockholm University, Roslagstullsbacken 23, SE-10691 Stockholm, Sweden*
[2]*Dipartimento di Fisica e Astronomia, viale Berti Pichat 6, I-40127 Bologna, Italy*
[3]*INAF, Osservatorio Astronomico di Bologna, via Ranzani 1, I-40127 Bologna, Italy*
[4] *Scuola Normale Superiore, Piazza dei Cavalieri 7, I-56126 Pisa, Italy*
[5]*Kavli IPMU (WPI), Todai Institutes for Advanced Study, the University of Tokyo, 5-1-5 Kashiwanoha, Kashiwa 277-8583, Japan*
[6]*Kavli Institute for Cosmology, University of Cambridge, Madingley Road, Cambridge CB3 0HA, UK*
[7]*Cavendish Laboratory, University of Cambridge, 19 J. J. Thomson Ave., Cambridge CB3 0HE, UK*

Accepted 2017 January 19. Received 2017 January 19; in original form 2016 June 18

**ABSTRACT**

With the aim of improving predictions on far-infrared (FIR) line emission from Giant Molecular

dynamical times (Bertoldi 1989; Bertoldi & McKee 1990; Gorti & Hollenbach 2002; Krumholz et al. 2006).

Besides extreme UV (EUV), ionizing ($h\nu < 13.6$ eV) photons, far-ultraviolet (FUV) photons ($6 < h\nu < 13.6$ eV) also strongly affect the chemistry, thermal balance, structure and dynamics of GMCs. FUV radiation dissociates molecular gas beyond the H II region, creating photodissociation regions (PDRs; Hollenbach & Tielens 1999) from which most infrared (IR) emission of galaxies originates. Dust grains and polycyclic aromatic hydrocarbons absorb radiation from the stars and re-radiate this energy in the IR; at the same time, photoelectrons heat the gas (Wolfire et al. 2003). Radiative cooling is enabled by many far-infrared (FIR) lines. The importance of FIR line emission in constraining the ISM properties (e.g. gas temperature, density and metallicity) has driven the advances in the IR and sub-millimeter astronomy. Nowadays, with the Atacama Large Millimeter/Submillmeter Array (ALMA), we can aim at constraining the properties of PDRs and those of the associated molecular clouds in the first galaxies. One of the primary goals of ALMA is the detection of the (redshifted) [C II] from the high-$z$ Universe (e.g. Carilli & Walter 2013), even though the physical interpretation of the line measurement from high redshifts is often very challenging (Maiolino et al. 2015; Gallerani et al. 2016; Knudsen et al. 2016). Many recent efforts (Nagamine, Wolfe & Hernquist 2006; Vallini et al. 2013, 2015; Olsen et al. 2015; Pallottini et al. 2015, 2017; Gallerani et al. 2016) have been devoted to relate the physical properties of neutral and molecular gas in high-$z$ galaxies to the FIR line luminosity. However, radiative feedback effects have not yet been included in such relation. Here we aim at making this step.

Our plan is to model the time evolution of FIR line emission from a single GMC illuminated by nearby massive stars. Our investigation builds upon previous studies (Bertoldi 1989; Bertoldi & McKee 1990; Gorti & Hollenbach 2002) on GMC photoevaporation (PE) induced by externally produced EUV/FUV photons impinging on the cloud. We adopt their analytic formalism to model the PE process and compute the time evolution of the GMC density field. Then, by coupling the model with the photoionization/photodissociation code CLOUDY, we self-consistently calculate the evolving luminosity of several FIR lines. Among these, the [C II] 158 μm fine structure line is often the most luminous, and it is considered the work-horse for high-$z$ galaxy exploration. We focus our attention also on [O III] at 88 μm, originating from the outer, ionized shell. The final goal is to assess whether (and how) PE, by affecting the density field of the GMCs, modulates FIR line emission under a range of different metallicity and irradiation conditions.

This paper is structured as follows: In Section 2, we describe how we model (i) the internal structure of the GMCs, and (ii) the radiation field impinging on the clouds. Then, we treat the PE theory in Section 3 presenting the model results. In Section 4, we show how the evolving density field in GMCs impacts FIR line emission. We draw our conclusions in Section 5, where some caveats are also discussed.

## 2 MODEL

A schematic description of our model is shown in Fig. 1. We consider an idealized case of a clumpy, starless GMC immersed in an external radiation field. The effects of gas clumpiness on the PDR structure and the resulting FIR line emission have been studied also by Meixner & Tielens (1993). Those calculations, however, do not account for the time evolution of the density field and feedback effects. The key features entering our model are (i) the GMC density structure, and (ii) the radiation field. These are discussed in detail in the following sections.

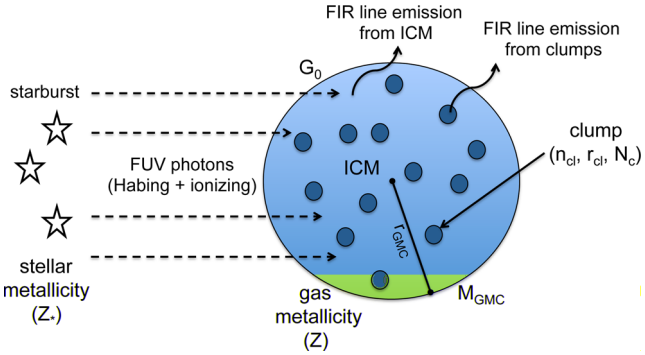


**Figure 1.** Sketch of the GMC model used in this work.

### 2.1 GMC density structure

Molecular clouds are observed to have a hierarchical structure with a density field showing enhancements (usually referred to as clumps and filaments) on ≈0.1–10 pc scales. The typical hydrogen column density of a GMC is $N_{\rm H} \approx 10^{22}$ cm$^{-2}$ (e.g. McKee & Ostriker 2007, and references therein), but variations are observed in the range $N_{\rm H} \approx 10^{21}-10^{23}$ cm$^{-2}$. GMCs are supported against collapse by turbulence and magnetic fields.

Numerical and analytical studies conclude that the probability distribution function (PDF) of the gas density, $\rho$, in a supersonically turbulent, isothermal cloud of mean density $\rho_0$ is lognormal:

$$g_s {\rm d}s = \frac{1}{\left(2\pi\sigma_s^2\right)^{1/2}} \exp\left[-\frac{1}{2}\left(\frac{s-s_0}{\sigma_s}\right)^2\right], \quad (1)$$

with $s \equiv \ln(\rho/\rho_0)$ (e.g. Vazquez-Semadeni 1994; Kim, Ostriker & Stone 2003; Krumholz & McKee 2005; Wada 2008; Tasker & Tan 2009; Hennebelle & Chabrier 2011, 2013; Padoan & Nordlund 2011; Federrath & Klessen 2013). The mean logarithmic density ($s_0$) is related to the standard deviation of the distribution ($\sigma_s$) by $s_0 = -\sigma_s^2/2$, which, in turn, depends on the sonic Mach number ($\mathcal{M}$) and the ratio of thermal to magnetic pressure ($\beta$) as

$$\sigma_s^2 = \ln\left(1 + b^2\mathcal{M}^2\frac{\beta}{\beta+1}\right). \quad (2)$$

The $b$ factor in the above equation parametrizes the kinetic energy injection mechanism (often referred to as forcing) driving the turbulence ($b \approx 0.3$–1; see Molina et al. 2012, for an extensive discussion).

When self-gravity is included, the PDF develops a power-law tail ($p_s \propto \rho^{-\kappa}$) at high densities. The occurrence of the power-law tail is confirmed both theoretically (e.g. Krumholz & McKee 2005; Hennebelle & Chabrier 2011; Padoan & Nordlund 2011; Federrath & Klessen 2013) and observationally via dust extinction measurements (e.g. Kainulainen et al. 2009; Lombardi, Alves & Lada 2015; Schneider et al. 2016; Stutz & Kainulainen 2015) or molecular line detections (e.g. Goldsmith et al. 2008; Goodman, Pineda & Schnee 2009; Schneider et al. 2016) carried out in nearby GMCs. While dust extinction allows us to probe a larger dynamic range [a measured visual extinction $A_V = 1-100$ mag corresponds to clump column densities ($N_{\rm cl}$) in the range $N_{\rm cl} \approx 10^{21}-10^{23}$ cm$^{-2}$], molecular line detections are limited to the high-density tail of the PDF ($N_{\rm cl} > 10^{23}$ cm$^{-2}$). Here we consider three different cloud models

**Table 1.** Properties of the GMC models considered in this work.

| Model | $M_{\rm GMC}$ ($M_\odot$) | $r_{\rm GMC}$ (pc) | $\mathcal{M}$ | $\rho_0$ (g cm$^{-3}$) |
|---|---|---|---|---|
| A | $6.2 \times 10^3$ | 4 | 10 | $8.2 \times 10^{-22}$ |
| B | $9.9 \times 10^4$ | 16 | 20 | $2.1 \times 10^{-22}$ |
| C | $3.9 \times 10^6$ | 100 | 50 | $3.3 \times 10^{-23}$ |

(named A, B and C, with properties summarized in Table 1) in order to bracket the range of values observed in Galactic GMCs, and those assumed in simulations by Federrath & Klessen (2013).

We set up the internal density of the clouds so that their PDFs are in agreement with those found by Federrath & Klessen (2013) for $\mathcal{M} = 10,\ 20$ and 50, mean gas density $\rho_0 = 8.2 \times 10^{-22},\ 2.1 \times 10^{-22}$ and $3.3 \times 10^{-23}$ g cm$^{-3}$, and turbulence forcing parameter $b \approx 0.3$. In Fig. 2, we show the PDF that has been fitted with a lognormal ($g_{\rm s}$, equation 1) function + power-law ($t_{\rm s}$) tail, i.e. $p_{\rm s} = g_{\rm s} + t_{\rm s}$. In what follows, we identify two components in the GMC, referred to as *clumps* and diffuse *interclump medium* (ICM), adopting a criterion based on the density PDF. We use the term *clumps* to denote small-scale structures ($< 1$ pc in size) that are part of the power-law tail. In the literature, clumps have been interpreted either as temporary density fluctuations produced by supersonic turbulence (Falgarone & Phillips 1990) or as stable physical entities confined by ICM pressure (Williams, Blitz & Stark 1995). Even though clump morphology is observed to vary from filamentary to quasi-spherical shapes, in our work, we model the clumps as spheres (see Fig. 1).

The volume filled by the gravitationally unstable clumps in the GMCs is

$$V_{\rm clumps} = V_{\rm GMC} - V_{\rm ICM}, \tag{3}$$

where the volume of the ICM is given by the lognormal distribution

$$V_{\rm ICM} = V_{\rm GMC} \int g_{\rm s}\, {\rm d}s. \tag{4}$$

We obtain $\int g_{\rm s}\, {\rm d}s = 0.94, 0.97$ and 0.98 for models A, B and C, respectively (see Fig. 2). To build the internal density field, we then use the following procedure:

(1) Randomly extract from the tail $t_{\rm s}$ the $i$th clump with number density[1] $n_{{\rm cl},\,i} = \rho/(\mu m_{\rm p})$.

(2) Calculate the clump radius as the turbulent Jeans length:

$$r_{{\rm cl},i} = \frac{1}{2}\lambda_{J,{\rm turb}} = \frac{1}{2}\frac{\pi\sigma^2 + \sqrt{36\pi c_{\rm s}^2 GL^2\rho + \pi^2\sigma^4}}{6GL\rho}, \tag{5}$$

where $c_{\rm s}$ is the sound speed. Equation (5) is obtained by using an effective (turbulent+thermal) pressure term in the Jeans length equation (see equations 35 and 36 in Federrath & Klessen 2012).

(3) Calculate the clump volume $V_{{\rm cl},i} = (4/3)\pi r_{{\rm cl},i}^3$.

(4) Iterate steps 1–3 until $\Sigma_i V_{{\rm cl},\,i} = V_{\rm clumps}$.

Finally, we compute the total mass in clumps $M_{\rm tot,cl} = \Sigma_i \frac{4}{3}\pi\mu m_{\rm p} n_{{\rm cl},i} r_{{\rm cl},i}^3$, the ICM total mass $M_{\rm ICM} = M_{\rm GMC} - M_{\rm tot,\,cl}$ and the ICM mean density $\langle n_{\rm ICM}\rangle = M_{\rm ICM}/(\mu m_{\rm p} V_{\rm ICM})$. The resulting clump distributions are shown with magenta crosses in Fig. 2. For models A, B and C, we find $M_{\rm tot,cl} \approx 1.2 \times 10^3,\ 1.8 \times 10^4$ and $7.2 \times 10^5\ M_\odot$, and $\langle n_{\rm ICM}\rangle \approx 651,\ 161$ and 26 cm$^{-3}$, respectively.

[1] We assume the gas to be a mixture of hydrogen and helium with mean molecular weight $\mu = 1.22$.

### 2.2 Radiation field

The spectral energy distribution (SED) of the radiation field impinging on the GMC surface is calculated using the stellar population synthesis code STARBURST99 (Leitherer et al. 1999), assuming a Salpeter initial mass function in the range 1–100 $M_\odot$. We adopt the Geneva standard evolutionary tracks (Schaller et al. 1992) with metallicity $Z_* = 1$, 0.2 and 0.05 $Z_\odot$, and Lejeune–Schmutz stellar atmospheres, which incorporate plane-parallel atmospheres and stars with strong winds (Schmutz, Leitherer & Gruenwald 1992; Lejeune, Cuisinier & Buser 1997). We follow the time evolution of the SED between 1 and 100 Myr considering a continuous SF mode. The star formation rate ( SFR) is a free parameter of the model. As an example, we show the SED for SFR $= 1\,M_\odot$ yr$^{-1}$ and $Z = 0.2\,Z_\odot$ in Fig. 3. The lines are colour-coded as a function of the starburst age. The grey shaded region highlights the non-ionizing FUV Habing band relevant to the PDR modelling; the strength of the FUV radiation is usually parametrized by $G_0$, the ratio of the FUV flux to the one measured by Habing (1968) in the Milky Way ($\approx 1.6 \times 10^{-3}$ erg cm$^{-2}$ s$^{-1}$). As expected for a continuous SF mode, the specific luminosity in the Habing band increases with time before saturating to an asymptotic value around 100 Myr.[2]

## 3 PHOTOEVAPORATION

The UV radiation produced by massive OB stars influences the structure, dynamics, chemistry and thermal balance of the surrounding gas. UV photons substantially alter the clump–interclump structure of GMCs: EUV and/or FUV photons heat the surface layer of clumps to high temperatures, causing the loss of their cold molecular mass that is ionized and/or photodissociated, and then it is converted into warm ionized/atomic gas (Hollenbach & Tielens 1999). This process is called *photoevaporation*. When the GMC is embedded in an H II region, the ICM is exposed to both EUV and FUV photons, while the internal clumps see only the attenuated FUV radiation. Penetration of EUV and FUV photons in the ICM and clumps is further addressed in Appendix A. There we show the temperature, $x_{\rm H_I}$, and $G_0$ profiles obtained with photoionizaton simulations discussed in detail in Section 3.2.

### 3.1 Analytical approach

Gorti & Hollenbach (2002) show that the evolution of a turbulent clump, impulsively irradiated by FUV photons, is influenced by only two parameters: (1) the ratio of the clump initial column density ($n_{\rm cl}^0 r_{\rm cl}^0$) to the column ($N_0$) penetrated by the FUV radiation,

$$\eta_0 \equiv \frac{n_{\rm cl}^0 r_{\rm cl}^0}{N_0}, \tag{6}$$

i.e. the depth into the cloud where $\tau_{FUV} \approx 1$; and (2) the strength of the FUV field, parametrized by the ratio of the sound speed in the FUV-heated region ($c_{\rm PDR}$) to the sound speed of the clump in the no-field case[3]:

$$\nu \equiv c_{\rm PDR}/c_{\rm c}. \tag{7}$$

[2] The SED can be approximated as a power law of the form $\log L_\lambda = \alpha \log\lambda$ + constant for $\lambda > 912$ Å. At the times relevant for PE, we find $\alpha = -2.2$ (age 1 Myr) and $-2.4$ (age 10 Myr).

[3] The parameter $\nu$ is therefore proportional to the square root of the ratio of the gas temperature in the PDR ($T_{\rm PDR}$) to the initial temperature of the clump ($T_{\rm c}$).

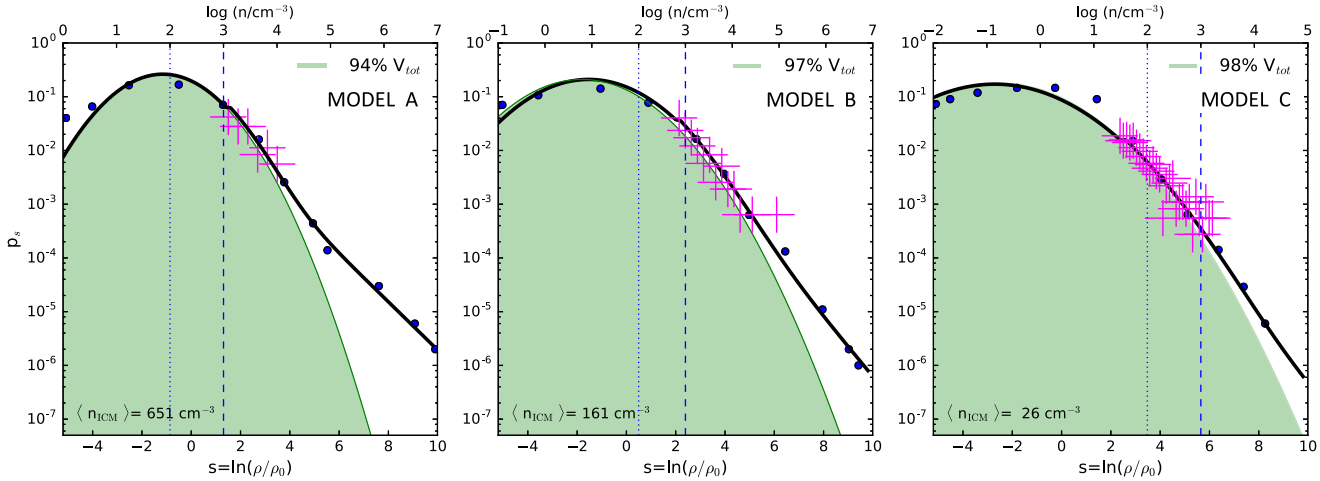


**Figure 2.** Volume-weighted PDFs (blue points) of the logarithmic density $s \equiv \ln(\rho/\rho_0)$ simulated by Federrath & Klessen (2013) for GMC models A, B and C in Table 1. The solid black line is the best lognormal + power-law fit to the numerical results. The volume fraction filled by the lognormally distributed gas (green area) is given for each model. The upper $x$-axis provides the gas number density $n$, along with the reference values $n = 10^2$ and $10^3$ cm$^{-3}$. Magenta crosses show the density of sampled GMC clumps (see Section 2.1 for details on the procedure adopted).

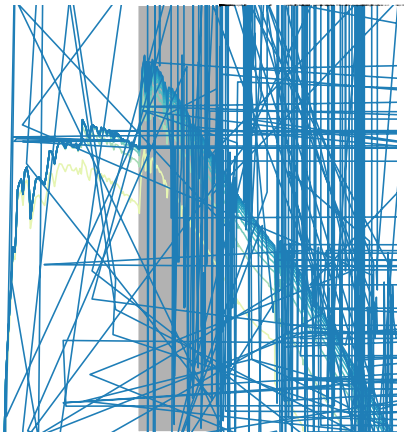

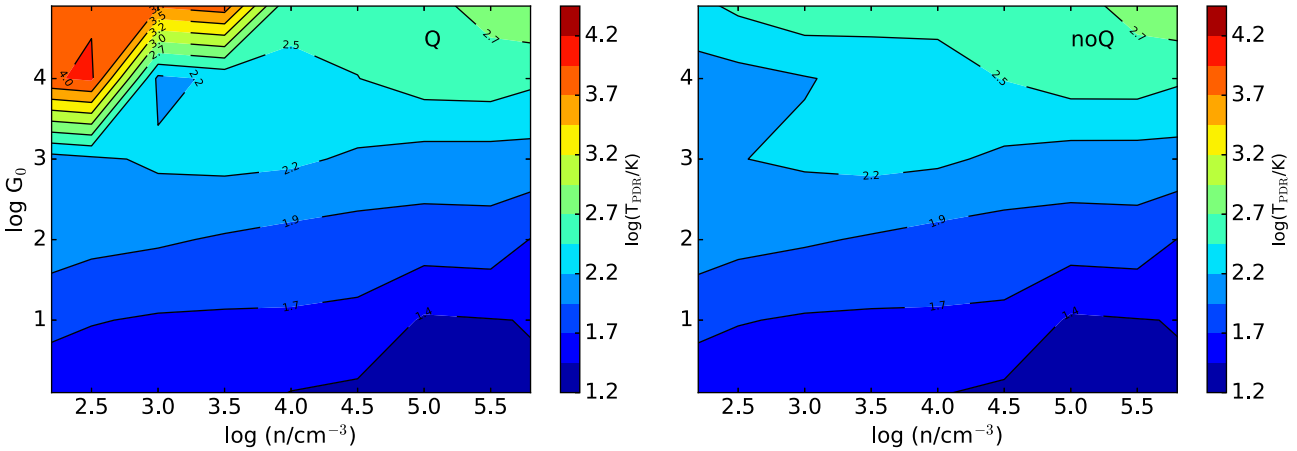


**Figure 5.** PDR temperature as a function of the gas density, $n$, and Habing flux, $G_0$, for `Q models` (left-hand panel) and `noQ models` (right-hand panel) for a solar metallicity gas. $T_{\rm PDR}$ is measured where the FUV ($\lambda_{\rm ref} = 1000$ Å) optical depth $\tau_{\rm FUV} = 1$.

We calculate $N_0$ and $T_{\rm PDR}$ with version c13.03 of CLOUDY (Ferland et al. 2013), which allows us to model the transition between the H II region, PDR and molecular part of a gas slab illuminated by a given radiation field. For each of the three metallicities[5] considered in this work ($Z = 0.05,\ 0.2$ and $1\,{\rm Z}_{\odot}$), we run two sets of simulations with different prescriptions for the external radiation spectrum: (i) a full spectrum (`Q models`) including both FUV and EUV photons, and (ii) a FUV spectrum only (`noQ models`). `Q models` (`noQ models`) is designed to mimic the flux reaching the GMC placed within (outside) an H II region.

We run a total of $66 \times 3$ CLOUDY simulations for each metallicity, and for $\log(n/{\rm cm}^{-3}) = [1{-}6]$ (in steps of 0.5 dex) and $\log G_0 = [0{-}5]$ (1 dex). The parameter space covers the plausible range of clumps/ICM densities (see Section 2.1), and Habing fluxes in galaxies. The code computes the radiative transfer through the slab up to a hydrogen column density $N_{\rm H} = 10^{23}\,{\rm cm}^{-2}$. This stopping criterion is chosen to (i) cover the whole range of column densities of our randomly generated clumps, and (ii) fully sample the molecular part of the illuminated slab, typically located at $N_{\rm H} \gtrsim 2 \times 10^{22}\,{\rm cm}^{-2}$.

We adopt the gas-phase abundances (${\rm C/H} = 3.0 \times 10^{-4}$, ${\rm O/H} = 4.0 \times 10^{-4}$, ${\rm Mg/H} = 3.0 \times 10^{-6}$, ${\rm N/H} = 7.0 \times 10^{-5}$, ${\rm S/H} = 1 \times 10^{-5}$) provided by CLOUDY for the Orion nebula (Rubin et al. 1991; Osterbrock, Tran & Veilleux 1992; Rubin, Dufour & Walter 1993),[6] scaled with the metallicity of each specific model. The model accounts for the cosmic microwave background (CMB) background at $z = 6$, which can suppress the emergent line luminosity of FIR lines when observed in contrast with the CMB (Gong et al. 2012; da Cunha et al. 2013; Pallottini et al. 2015; Vallini et al. 2015; Zhang et al. 2016). In the calculation, we consider a cosmic-ray (CR) ionization rate $\zeta_{\rm CR} = 2 \times 10^{-16}{\rm s}^{-1}$ (Indriolo et al. 2007). Note, as a caveat, that the variation of the CR ionization rate has strong effects on the chemistry and emission of PDRs (e.g. Bayet et al. 2011; Meijerink et al. 2011; Papadopoulos et al. 2011; Bisbas, Papadopoulos & Viti 2015).[7] The CRs, unlike FUV radiation, travel nearly unimpeded through the clouds and provide a source of input energy by (i) freeing electrons, and (ii) inducing an internal UV field through the excitation of $H_2$ (see also Indriolo & McCall 2013, and references therein).

In Fig. 5, we plot $T_{\rm PDR}$ as a function of the gas number density ($n$) and Habing flux ($G_0$) for $Z = {\rm Z}_{\odot}$, where the FUV ($\lambda_{\rm ref} = 1000$ Å) optical depth $\tau_{\rm FUV} = 1$. This criterion is chosen because the temperature $T_{\rm PDR}$ entering in the Gorti & Hollenbach (2002) model (see Section 3) refers to the FUV-heated region, i.e. extending up to the point at which the FUV optical depth reaches a value of the order of unity.

The PDR temperatures obtained with `Q models` and `noQ models` are similar, apart from low-density ($n < 10^3\,{\rm cm}^{-3}$) and strong field ($G_0 > 10^3$) regimes, where `Q models` are warmer. The results are in agreement with those found by Kaufman et al. (1999) (see also fig. 19 in Visser et al. 2012). Furthermore, as a sanity check, we compare $T_{\rm PDR}$ with that obtained by Bothwell et al. (2017) using the 3D-PDR code (Bisbas et al. 2012). Bothwell et al. (2017) cover the same range of $G_0$ and $n$ considered here, but they sample the PDR temperature deeper into the gas slab ($A_V = 3$). As expected, our results ($T_{\rm PDR} \approx 10^{1.2}{-}10^{2.5}$ K, in the range $G_0 = [10^0{-}10^4]$ and $n = [10^2{-}10^5]\,{\rm cm}^{-3}$) are slightly higher than those ($T_{\rm PDR} \approx 10^{1.1}{-}10^{2.0}$ K) found by Bothwell et al. (2017) (see their fig. 10) in the same range of $n$ and $G_0$.

Once the PDR temperature and column density as a function of $n$ and $G_0$ are known, we can determine the values of $\eta_0$ and $\nu$ for each cloud. This allows us to compute the time evolution of their mass, density and radius (see Appendix B). At each time-step $t_i$, we update the value of $\eta_0$ and $\nu$ according to the clump density at the previous time-step, $n_{\rm cl}(t_{i-1})$, assuming that $G_0$ is constant with time (Visser et al. 2012; Bothwell et al. 2017).

[5] We do not make a distinction between gas and stellar metallicities, which are then supposed to be equal.

[6] As a caveat, we note that, in the standard CLOUDY set for the Orion nebula, the carbon and oxygen abundances provided are ≈2 and ≈1.5 times greater than the values reported by, e.g. Cardelli et al. (1996, ${\rm C/H} = 1.4 \times 10^{-4}$) and Cartledge et al. (2004, ${\rm O/H} = 2.8 \times 10^{-4}$), respectively.

[7] The effect of the variation of $\zeta_{\rm CR}$ on the [C II] (CO) line intensity has been quantified by, e.g. Meijerink et al. (2011), who show that for a PDR of density $n = 10^3\,{\rm cm}^{-3}$, irradiated by $G_0 = 10^3$, $I_{\rm C\,II} = [4.4{-}8.6] \times 10^{-4}\,{\rm erg\,s^{-1}sr^{-1}}$ ($I_{\rm CO} = [7.6{-}0.28] \times 10^{-8}\,{\rm erg\,s^{-1}sr^{-1}}$) when varying $\zeta_{\rm CR} = 5 \times [10^{-17}{-}10^{-14}]\,{\rm s}^{-1}$. Recently, Bisbas et al. (2015) have argued that CR-induced destruction of CO in GMCs is likely the single most important factor controlling the CO visibility in star-forming galaxies.

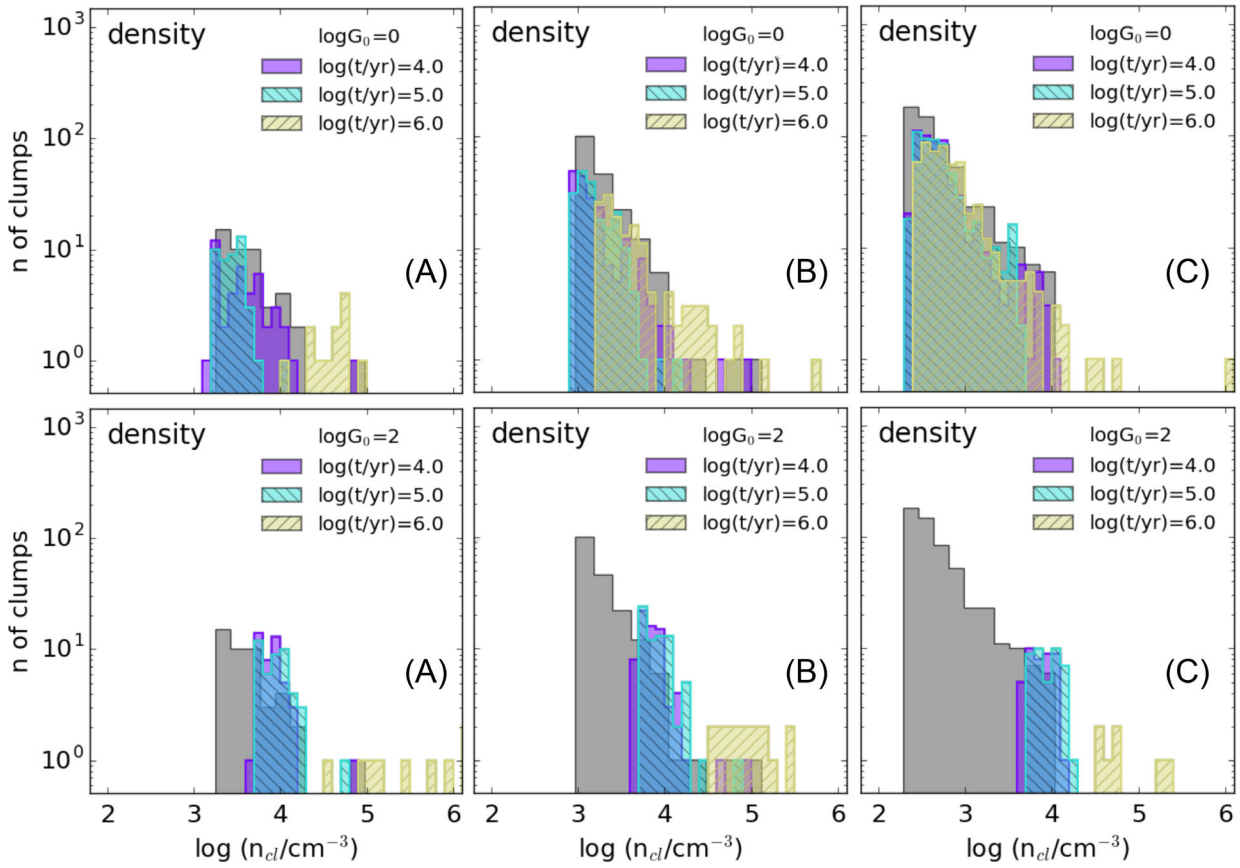


**Figure 6.** Time evolution of the clump density distributions for models A, B and C as a function of $G_0$ at the clump surfaces ($\log G_0 = 0$ and 2, top and bottom rows, respectively). The distributions at $t = 10^4$, $10^5$ and $10^6$ yr are shown with transparent coloured histograms, and the initial distribution is shown in solid grey. Photoevaporated clumps are removed from the distribution.

### 3.3 Clump PE

Figs 6 and 7 show the time evolution of the clump density and mass distribution for the three model clouds A, B and C. We concentrate on the effect $G_0$ variations on clump PE at a fixed metallicity, $Z = Z_\odot$. We define a clump as completely photoevaporated at time $t$, and hence removed from the clump inventory, if one of the two following conditions is satisfied: (i) the radius $r_{\rm cl}(t) = 0$, or (ii) the clump density $n_{\rm cl}(t) = \langle n_{\rm ICM} \rangle$, i.e. the clumps become indistinguishable from the ICM. For $\log G_0 = 0$, the PE proceeds mainly via expansion. The density distribution shifts towards lower values. However, a small fraction (<1 per cent in mass, see Fig. 7) of longer lived, compressed clumps is visible in the high-density tail at $t = 10^6$ yr. In contrast, for $\log G_0 = 2$, PE proceeds via shock compression for all the clumps, and the distribution shifts towards higher densities. These trends hold for both models A and B; model C is initially less dense (see Fig. 2), and the compression mode becomes important already for $\log G_0 = 0$.

During PE, mass-loss takes place, and a certain fraction of the clump mass is returned to the ICM. For $\log G_0 = 0$, such fraction after $10^4$ yr is $f_4 = 0.77$–$0.88$ depending on the cloud model; for $\log G_0 = 2$, mass-loss is more substantial, i.e. $f_4 = 0.78$–$0.99$. We note that at a fixed $G_0$ at the clump surface, $f_4$ and $f_6$ (the analogous fraction after 1 Myr) increase going from model A to model B to model C, along their decreasing clump density sequence.

### 3.4 ICM PE

ICM PE is computed with a procedure similar to that adopted for the clumps. However, for the ICM, the effects of EUV photons become important if the GMC is located within an H II region. For example, consider the case $\log G_0 \geq 5$ and $Z = Z_\odot$. Then, the typical column density of the H II layer in a gas of $n \approx 100\,{\rm cm}^{-3}$ is $N_{\rm H\,II} \approx 10^{22}\,{\rm cm}^{-2}$ (see Fig. A1, and the discussion in Appendix A), and thus comparable to the ICM column density. This implies that the GMC is almost fully ionized, and that PE is driven by the increased temperature ($T_{\rm H\,II} \approx 10^4$ K) in the ionized layer.

To model this regime, we adopt a modified version of the PE equations in Appendix B. In the equations for the time evolution of radius, mass and density, we replace the parameter $\eta_0$ (see equation 6) with

$$\eta_0^{\rm H\,II} \equiv \frac{n_{\rm ICM}\, r_{\rm GMC}}{N_{\rm H\,II}}, \tag{9}$$

where $N_{\rm H\,II}$ is the column density of the H II layer. Moreover, we substitute $\nu$ (see equation 7) with

$$\nu^{\rm H\,II} \equiv \frac{c_{\rm H\,II}}{c_{\rm c}}, \tag{10}$$

where $c_{\rm H\,II}$ is the sound speed in the ionized layer. Note that $\nu_{\rm H\,II} > \nu$, due to the higher temperature in the H II region with respect to PDRs. As in the case of clumps, $\eta_0^{\rm H\,II}$ and $\nu_{\rm H\,II}$ depend on $N_{\rm H\,II}$ and $T_{\rm H\,II}$, which have been determined from CLOUDY simulations at the depth at which the gas is 50 per cent ionized. We follow the evolution

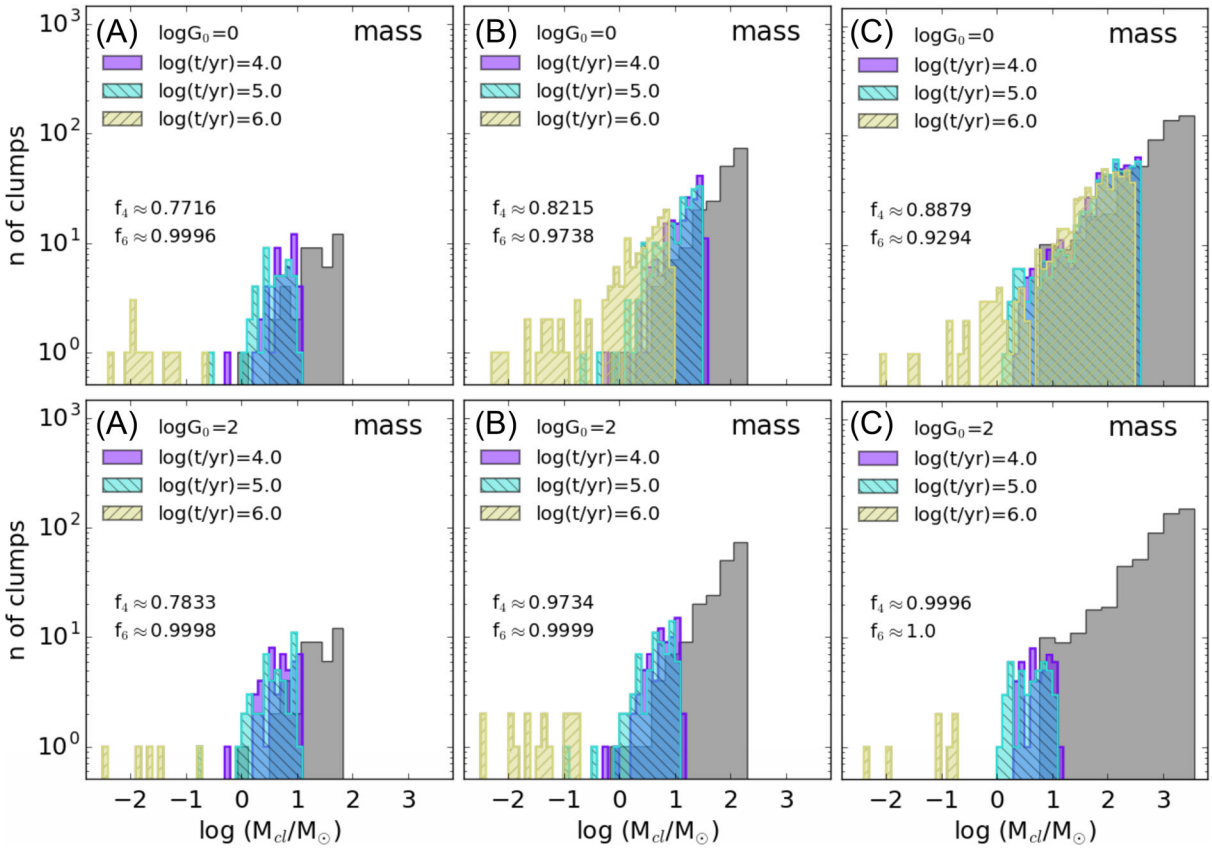


**Figure 7.** Same as Fig. 6 but for the clump mass distribution. The fraction of mass returned to the ICM at $t = 10^4$ and $10^6$ yr ($f_4$ and $f_6$, respectively) is given in each panel.

of ICM density, GMC radius and mass until complete GMC PE, defined by one of the two criteria: (i) $M_{\rm ICM} < 10$ per cent $M_{\rm GMC}$, or (ii) the ICM density falls below $\approx$10 cm$^{-3}$, i.e. the typical density of the diffuse cold neutral ISM phase (Wolfire et al. 2003).

### 3.5 GMC PE time-scales

In Fig. 8, we plot the GMC PE time ($t_{\rm pe}$) as a function of $G_0$ for different metallicities, $Z = 1$, 0.2 and 0.05 Z$_\odot$. At a fixed cloud mass and $G_0$, a decreasing $Z$ results in a faster PE. This trend is mostly driven by the decreasing dust-to-gas ratio allowing the deeper UV radiation penetration to heat the internal gas layers. As a final remark, we note that for $Z = $ Z$_\odot$, the maximum $t_{\rm pe} \approx 30$ Myr in model B is consistent with the results by Williams & McKee (1997) and Krumholz et al. (2006). These authors find $t_{\rm pe} \approx 30-40$ Myr for GMCs of mass $10^5$M$_\odot$ when considering the PE produced by OB associations *inside* the GMC.

## 4 FIR LINE EMISSION

From our model, we now compute the FIR line emission from GMCs, including the effects of PE. At each time-step in the computation, we derive the line luminosity of the clumps (ICM) depending on their actual density, $n_{\rm cl}(t)$ ($n_{\rm ICM}(t)$), emitting area, $\pi r_{\rm cl}(t)^2$ ($\pi r_{\rm GMC}(t)^2$) and column density $N_{\rm cl}(t) = n_{\rm cl}(t) r_{\rm cl}(t)$ ($N_{\rm ICM}(t) = n_{\rm ICM}(t) r_{\rm GMC}(t)$). Again, we use CLOUDY to compute the FIR line flux, $I_{\rm line}(n, G_0, N_{\rm H})$ (in erg s$^{-1}$ cm$^{-2}$), at the relevant surface (clump/ICM). The total luminosity is calculated as a sum over the clumps and the ICM:

$$L_{\rm line}(t) = \sum_{cl} I_{\rm line}\left(\langle f_{\rm att}\rangle G_0, n_{\rm cl}(t), N_{\rm cl}(t)\right) \pi r_{cl}^2(t) + I_{\rm line}\left(G_0, n_{\rm ICM}(t), N_{\rm ICM}(t)\right) \pi r_{\rm GMC}^2(t). \quad (11)$$

In the above expression, the UV flux seen by the clumps is attenuated by the ICM by an average factor $\langle f_{\rm att}\rangle = G_0(\langle N_{\rm H}\rangle)/G_0$ to roughly account for the GMC-scale radiative transfer effects not included here. The mean absorbing column density to each clump is $\langle N_{\rm H}\rangle \approx 0.25\, r_{\rm GMC}\, n_{\rm ICM}$. For models A, B and C, we get $\langle N_{\rm H}\rangle \approx 2 \times 10^{21}$ cm$^{-2}$, yielding $\langle f_{\rm att}\rangle \approx 0.2, 0.72$ and 0.9 for $Z = 1, 0.2$ and 0.05 Z$_\odot$. See Appendix A for further discussion on this point.

The predicted specific (i.e. per unit mass of emitting material) [C II] luminosity, $\epsilon_{\rm C\,II}$, is shown in Fig. 9 for the different cloud models. Such predictions are in very good agreement with recent observations, for example, of the Orion Molecular Cloud 1 (OMC1) by Goicoechea et al. (2015). The observed total mass in the OMC1 region is $M_{\rm gas} = 2600$ M$_\odot$, thus comparable with $M_{\rm GMC}$ in model A. Additionally, Goicoechea et al. (2015) measured a mean value of $G_0 \simeq 2 \times 10^4$, and a specific luminosity $L_{\rm C\,II}/M_{\rm gas} = 0.16$ L$_\odot$/M$_\odot$. This is consistent with our predictions for the same $G_0$ at $Z = $ Z$_\odot$ (Fig. 9, upper-/left-hand panel). As $\epsilon_{\rm C\,II}$ is almost independent of the GMC model, in the rest of the discussion, we will refer to the fiducial GMC case, i.e. model B.

### 4.1 [C II] line emission

In Fig. 10, we plot the [C II] luminosity for model B as a function of $G_0$, and time, $t$, elapsed from the onset of the cloud illumination by a nearby starburst. The [C II] line has critical densities $n^{\rm e}_{\rm crit} \approx 50$ cm$^{-3}$

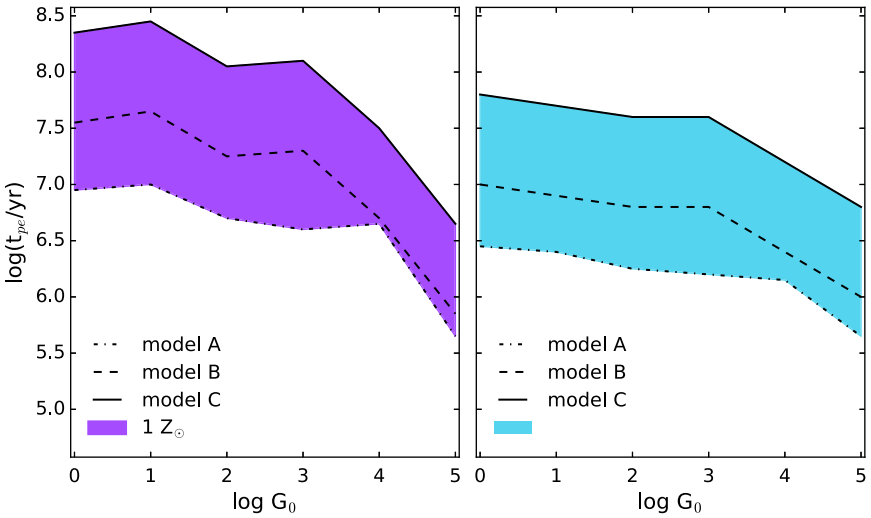

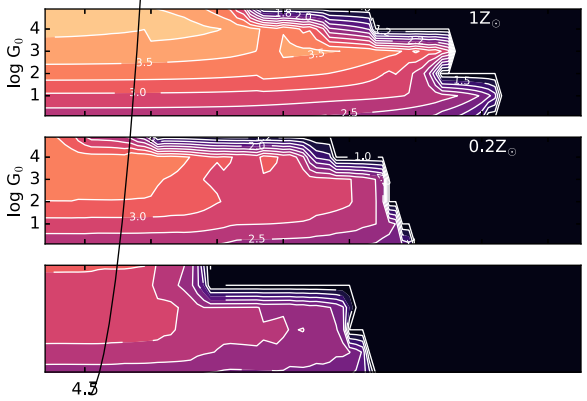
1Z⊙
0.2Z⊙
log G₀
4
3
2
1
3.5
3.0
2.5
2.0
1.0
4.5

**Table 2.** The coefficients of the polynomial fit for the [C II] and [O III] specific luminosities at $t = 10^5$ yr, as expressed in equation (12).

| Coefficients | [C II] specific luminosity | | | [O III] specific luminosity | | |
|---|---|---|---|---|---|---|
| | $Z = Z_\odot$ | $Z = 0.2\,Z_\odot$ | $Z = 0.05\,Z_\odot$ | $Z = Z_\odot$ | $Z = 0.2\,Z_\odot$ | $Z = 0.05\,Z_\odot$ |
| $\alpha$ | −2.424 | −2.476 | −2.652 | −2.616 | −9.079 | −9.661 |
| $\beta$ | 0.375 | 0.505 | 0.314 | −9.298 | 1.088 | 1.075 |
| $\gamma$ | 0.022 | −0.102 | −0.003 | 5.233 | 0.922 | 0.929 |
| $\delta$ | −0.009 | 0.007 | −0.015 | −0.694 | −0.168 | −0.168 |

of observational and simulated results, and (ii) their time evolution during the PE process.

By exploring UV field intensities (in Habing units) in the range $G_0 = 1$–$10^5$ and gas metallicities $Z = 1$, 0.2 and $0.05\,Z_\odot$, we find that the fiducial GMC (model B in Table 1) is completely photoevaporated in a time-scale $t_{\rm pe} \leq 30$ Myr. This time-scale is comparable to that deduced for destruction due to expanding H II regions around newborn stars inside GMCs (Williams & McKee 1997; Krumholz et al. 2006).

The PE time-scale is a decreasing function of metallicity, and it goes from 30 Myr at $Z = Z_\odot$ to 1 Myr at $Z = 0.05\,Z_\odot$ for the fiducial cloud. This is because the increased penetration of FUV leads to thicker and hotter PDRs leading to a faster PE. Due to similar physical reasons, at a fixed metallicity, $t_{\rm pe}$ decreases for higher FUV fluxes. The presence of ionizing EUV photons becomes important for low metallicities ($Z \leq 0.2\,Z_\odot$) and strong ($\log G_0 > 4$) radiation fields, when the column density of the ionized layer becomes comparable to the total GMC one.

We compute the evolution of [C II], and [O III] line luminosity during the PE process. We show that the [C II] emission per unit mass ($\epsilon_{\rm C\,II}$) for the three GMC models is independent of the internal GMC properties (i.e. the cloud model) and is a function of $G_0$ only, modulo a scaling factor $\propto t_{\rm pe}$ entering the time evolution. It is then possible to specialize our results to the fiducial case (model B) only.

FIR line luminosities depend on (i) time, $t$, elapsed from the onset of irradiation; (ii) metallicity, $Z$, of the GMC; and (iii) UV field intensity, $G_0$. Albeit the interplay of these parameters is complex, a well-defined general trend emerges. Stronger UV fluxes produce higher [C II] and [O III] luminosities, however, lasting for progressively shorter times (i.e. $t_{\rm pe}$ decreases along this sequence). More specifically, we find the following:

(1) For $Z = Z_\odot$, [C II] emission peaks at $t \lesssim 1$ Myr and $\log G_0 \geq 3$; the peak amplitude decreases towards lower metallicities. At fixed $Z$, the [C II] correlates with $G_0$, even though such trend is relatively mild and tends to flatten, particularly at a very low metallicity ($Z = 0.05\,Z_\odot$). Note that a GMC exposed to a low $G_0$ is less luminous, but its emission phase can last longer.

(2) Low metallicities ($Z \leq 0.2\,Z_\odot$) and high UV fluxes ($\log G_0 \approx 4$) maximize the [O III]/[C II] ratio, pushing it to values up to ≈1000. However, due to the shorter $t_{\rm pe}$, for a very low metallicity, such intense [O III] emission phase can be sustained only for $10^{5.4} \leq t \leq 10^{5.6}$ yr at $Z = 0.05\,Z_\odot$.

(3) The above results are consistent with recent observations of a Lyman Alpha Emitter (LAE) at $z \approx 7.2$ (Inoue et al. 2016), showing an [O III]/[C II] ratio >12 and $Z \approx 0.1\,Z_\odot$. Under these conditions, we find that gas metallicities $Z \leq 0.2\,Z_\odot$ allow to sustain [C II]/[O III] = 12 for $\approx 10^{6.5}$–$10^{6.7}$ yr.

Although physically solid, our model has some caveats. As SF within the GMC is not considered, the effects of internal radiation sources is not accounted for. Given that the SF efficiency per free-fall time, $\epsilon_{\rm eff}$, varies considerably in GMCs (e.g. Semenov, Kravtsov & Gnedin 2016, $\epsilon_{\rm eff} = 0.1$–10 per cent), the estimate of the actual number of OB stars depends strongly on the local conditions of the GMC. Williams & McKee (1997) estimate that for clouds of mass $10^5\,M_\odot$, about half are expected to contain at least one OB star. By the way, note that if an OB star forms in the GMC, the result of its ignition is to provide high UV fluxes to the cloud.[8] The PE time-scales for a GMC destroyed by an internal OB association that forms blister H II regions are $t_{\rm pe} \approx 30$–40 Myr (Williams & McKee 1997), which is comparable to that found with our modelling at solar metallicity.

To conclude, we have pointed out that the PE of GMCs dramatically affects their survival and FIR emission properties in a complex way. This has to be kept in mind when interpreting the FIR line data from high-$z$ galaxies, which are metal-poor and characterized by hard interstellar radiation fields, all conditions leading to fast PE. As already pointed out in Vallini et al. (2015), PE feedback might be responsible for the observed spatial displacement of FIR line-emitting sites with respect to the UV continuum position. In the central regions, in fact, GMC might be evaporated by the powerful radiation field, with the result that FIR lines are suppressed in the vicinity of the star-forming region. The impact of such effects on galactic scales will be explored in a forthcoming study.

## ACKNOWLEDGEMENTS

We thank the anonymous referees for their thorough and constructive comments that have greatly improved this paper. We are indebted to D. Cormier, A. Citro, E. Sobacchi and F. Pacucci for useful comments. We thank all the participants of *The Cold Universe* programme held in 2016 at the KITP, UC Santa Barbara, for valuable comments and discussions during the workshop. This research was supported in part by the National Science Foundation under Grant No. NSF PHY11-25915.

## REFERENCES

Bayet E., Williams D. A., Hartquist T. W., Viti S., 2011, MNRAS, 414, 1583
Bertoldi F., 1989, ApJ, 346, 735
Bertoldi F., McKee C. F., 1990, ApJ, 354, 529
Bisbas T. G., Bell T. A., Viti S., Yates J., Barlow M. J., 2012, MNRAS, 427, 2100
Bisbas T. G., Papadopoulos P. P., Viti S., 2015, ApJ, 803, 37
Bonnell I. A., Dobbs C. L., Robitaille T. P., Pringle J. E., 2006, MNRAS, 365, 37
Bothwell M. S. et al., 2017, MNRAS, 466, 2825
Cardelli J. A., Meyer D. M., Jura M., Savage B. D., 1996, ApJ, 467, 334
Carilli C. L., Walter F., 2013, ARA&A, 51, 105
Cartledge S. I. B., Lauroesch J. T., Meyer D. M., Sofia U. J., 2004, ApJ, 613, 1037

[8] The Habing flux provided by an O star at ≈0.1 pc from its surface is $\log G_0 \approx 6$ (Hollenbach & Tielens 1999).

Cormier D. et al., 2012, A&A, 548, A20
Cormier D. et al., 2015, A&A, 578, A53
da Cunha E. et al., 2013, ApJ, 766, 13
Dale J. E., Ngoumou J., Ercolano B., Bonnell I. A., 2013, MNRAS, 436, 3430
Dale J. E., Ngoumou J., Ercolano B., Bonnell I. A., 2014, MNRAS, 442, 694
Elmegreen B. G., Scalo J., 2004, ARA&A, 42, 211
Falgarone E., Phillips T. G., 1990, ApJ, 359, 344
Federrath C., Klessen R. S., 2012, ApJ, 761, 156
Federrath C., Klessen R. S., 2013, ApJ, 763, 51
Ferland G. J. et al., 2013, Rev. Mex. Astron. Astrofis., 49, 137
Gallerani S., Pallottini A., Feruglio C., Ferrara A., Maiolino R., Vallini L., Riechers D. A., 2016, preprint (arXiv:1604.05714)
Goicoechea J. R. et al., 2015, ApJ, 812, 75
Goldsmith P. F., Heyer M., Narayanan G., Snell R., Li D., Brunt C., 2008, ApJ, 680, 428
Gong Y., Cooray A., Silva M., Santos M. G., Bock J., Bradford C. M., Zemcov M., 2012, ApJ, 745, 49
Goodman A. A., Pineda J. E., Schnee S. L., 2009, ApJ, 692, 91
Gorti U., Hollenbach D., 2002, ApJ, 573, 215
Habing H. J., 1968, Bull. Astron. Inst. Neth., 19, 421
Hennebelle P., Chabrier G., 2011, ApJ, 743, L29
Hennebelle P., Chabrier G., 2013, ApJ, 770, 150
Hollenbach D. J., Tielens A. G. G. M., 1999, Rev. Mod. Phys., 71, 173
Indriolo N., McCall B. J., 2013, Chem. Soc. Rev., 42, 7763
Indriolo N., Geballe T. R., Oka T., McCall B. J., 2007, ApJ, 671, 1736
Inoue A. K., Shimizu I., Tamura Y., Matsuo H., Okamoto T., Yoshida N., 2014, ApJ, 780, L18
Inoue A. K. et al., 2016, Science, 352, 1559
Kainulainen J., Lada C. J., Rathborne J. M., Alves J. F., 2009, A&A, 497, 399
Kaufman M. J., Wolfire M. G., Hollenbach D. J., Luhman M. L., 1999, ApJ, 527, 795
Kim W.-T., Ostriker E. C., Stone J. M., 2003, ApJ, 599, 1157
Kim J.-G., Kim W.-T., Ostriker E. C., 2016, ApJ, 819, 137
Knudsen K. K., Richard J., Kneib J.-P., Jauzac M., Clement B., Drouart G., Egami E., Lindroos L., 2016, MNRAS, 462, L6
Körtgen B., Seifried D., Banerjee R., Vázquez-Semadeni E., Zamora-Avilés M., 2016, MNRAS, 459, 3460
Krumholz M. R., McKee C. F., 2005, ApJ, 630, 250
Krumholz M. R., Matzner C. D., McKee C. F., 2006, ApJ, 653, 361
Leitherer C. et al., 1999, ApJS, 123, 3
Lejeune T., Cuisinier F., Buser R., 1997, A&AS, 125
Lombardi M., Alves J., Lada C. J., 2015, A&A, 576, L1
McKee C. F., Ostriker E. C., 2007, ARA&A, 45, 565
Mac Low M.-M., Klessen R. S., 2004, Rev. Mod. Phys., 76, 125

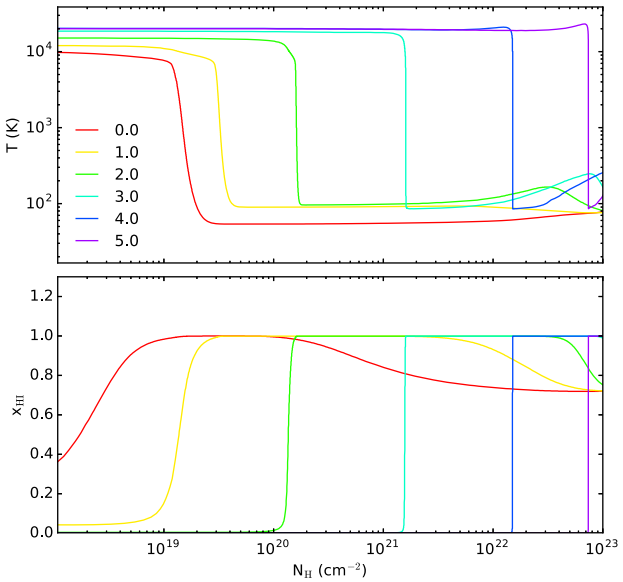


**Figure A1.** Temperature and $x_{H\,I}$ profiles obtained with CLOUDY when considering a gas slab characterized by $n = 100\,\mathrm{cm}^{-3}$ and illuminated by SED resulting from continuous SF at 1 Myr. The lines are colour-coded according to log $G_0$ at the gas slab surface.

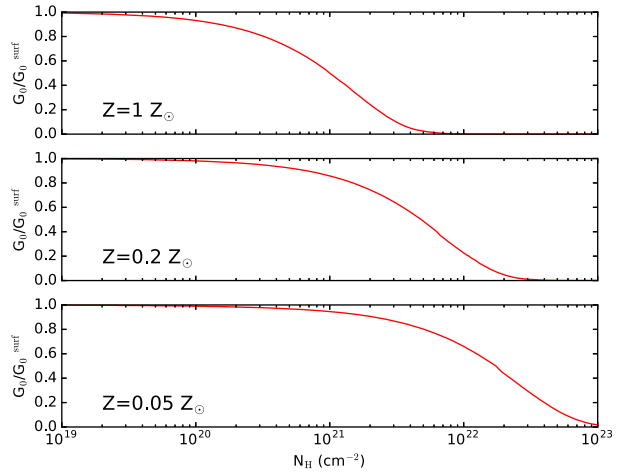


**Figure A2.** Profile of the $G_0$ attenuation as resulting from CLOUDY simulations considering a gas slab characterized by $n = 100\,\mathrm{cm}^{-3}$ and $Z = 1, 0.2$ and $0.05\,Z_\odot$ from top to bottom.

slab with $Z = 1\,Z_\odot$ are $N_{H\,II} \approx 4 \times 10^{21}\,\mathrm{cm}^{-2}$ for $G_0 = 10^4$ and $N_{H\,II} \approx 7 \times 10^{21}\,\mathrm{cm}^{-2}$ for $G_0 = 10^5$.

Note that above such column density, any H-ionizing photons are then absorbed in a thin ($N_H \approx 10^{19}\,\mathrm{cm}^{-2}$ or $\Delta A_V \approx 10^{-2}$) transition zone in which the ionization structure changes from being almost fully ionized ($x_e \approx 1$) to being almost fully neutral ($x_e \approx 10^{-4}$; Hollenbach & Tielens 1999).

In Fig. A2, we plot the attenuation of the Habing flux ($G_0/G_0^{surf}$) through the gas slab as a function of the metallicity. As we assume a dust-to-gas ratio that scales linearly with $Z$, at lower $Z$, it corresponds to a lower $G_0$ attenuation. These profiles are adopted to compute the average Habing field impinging the clump surfaces $\langle G_0^{clumps}\rangle = \langle f_{att}\rangle G_0^{surf}$, with

$$\langle f_{att}\rangle = G_0\left(\left\langle N_H^{ICM-clumps}\right\rangle\right)/G_0^{surf}, \tag{A3}$$

where $\langle N_H^{ICM-clumps}\rangle$ is the mean column of gas in the ICM between the GMC and the clump surfaces. $\langle N_H^{ICM-clumps}\rangle = n_{ICM}\langle l\rangle$ is calculated by sampling the location ($l$) of the clumps in the GMC via a Monte Carlo acceptance–rejection method by assuming (i) a uniform clump distribution, and (ii) the GMC to be spherical. The mean radius is $\langle l\rangle = 0.25 r_{GMC}$.

## APPENDIX B: PE MODEL

Clumps are assumed to be dense, small spheres of initial radius $r_{cl}^0$, and initial density $n_{cl}^0$, supported by thermal, turbulent and magnetic pressures. The magnetic field $B$ scales with a constant power of the density so that the magnetic pressure is $P_B \propto n^\gamma$. The ratios of turbulent, and magnetic, pressures to the thermal pressure are indicated with $\alpha \equiv P_{turb}/P_T$ and $\beta \equiv P_B/P_T$. The fiducial values in Gorti & Hollenbach (2002), kept fixed in our work, are $\alpha = \beta = 1$ and $\gamma = 4/3$.

### B1 Evolution of shock-compressed clumps

Let $r_{cl}(0) = r_{cl}^0 - \delta_0$, where $\delta_0 = N_0/n_{cl}^0$ is the initial thickness of the PDR shell on the surface of the clump. In the case of shock-compressed clumps, Gorti & Hollenbach (2002) demonstrated (cf. equations from B1 to B17 in their paper) that the shock compression shrinks the clump in a time $t_s \simeq r_{cl}(0)/c_{PDR}$ to a radius $r_s$. The clump mass at $t = t_s$ is

$$m_c(t_s) = m_{cl}(0) - 8\pi m_H N_0 r_{cl}(0)^2 \frac{v_b}{2c_{PDR}}, \tag{B1}$$

where $v_b \approx 0.7 c_{PDR}$ is the average velocity with which the radius decreases. After being compressed by the shock, the clump radius and mass evolve as

$$r_{cl}(t > t_s) = \left(\left[\left[\frac{r_s}{r_{cl}(0)}\right]^{2-1/\gamma} - \frac{2\gamma-1}{3\gamma-1}\frac{6\nu\eta_0}{(\eta_0-1)^2} \times \left[\frac{\beta(\eta_0-1)}{2(2\nu^2+\alpha)}\right]^{1/\gamma}\left[\frac{t}{t_c} - \frac{(\eta_0-1)}{\eta_0\nu}\right]\right)^{\gamma/(2\gamma-1)} \tag{B2}$$

and

$$m_{cl}(t > t_s) = m_{cl}(0)\left[\frac{2(2\nu^2+\alpha)}{\beta(\eta_0-1)^2}\right]^{1/\gamma}\left[\frac{r_{cl}(t)}{r_{cl}(0)}\right]^{3-1/\gamma}. \tag{B3}$$

The PE time-scale, obtained by setting the clump radius to zero, is

$$t_{pe} = t_c\left[\left[\frac{r_s}{r_{cl}(0))}\right]^{2-1/\gamma}\left(\frac{3\gamma-1}{2\gamma-1}\right) \times \frac{(\eta_0-1)^2}{6\nu\eta_0}\left[\frac{2(2\nu^2+\alpha)}{\beta(\eta_0-1)}\right]^{1/\gamma} + \frac{\eta_0-1}{\eta_0\nu}\right]. \tag{B4}$$

### B2 Evolution of clumps with initial expansion

Assuming that the clumps expand in the vacuum (cf. equations from C1 to C7 in Gorti & Hollenbach 2002) at their sound speed $c_c$ until the pressure drops to that in the heated outer layer, it is possible to demonstrate that the expansion time is

$$t_e = t_c\left(1 - \frac{1}{\eta_0}\right)\left[\left[\frac{3\nu+\eta_0-1}{3\nu 2(2\nu^2+\alpha)/(1+\alpha)}\right]^{1/2} - 1\right]. \tag{B5}$$

The time evolution of the clump radius and mass at $t > t_e$ is

$$r_{cl}(t > t_e) = r_{cl}(t_e) - \frac{3}{2} c_{PDR} \frac{1+\alpha}{2\nu^2+\alpha}(t - t_e) \quad \text{(B6)}$$

and

$$m_{cl}(t > t_e) = m_{cl}^0 \frac{2(2\nu^2+\alpha)}{\eta_0(1+\alpha)} \left[\frac{r_{cl}(t)}{r_c^0}\right]^2 . \quad \text{(B7)}$$

The PE time-scale is obtained by setting the clump radius to zero:

$$t_{pe} = \left(\frac{2\nu^2+\alpha}{1+\alpha}\right) \frac{r_{cl}(0) + c_c t_e}{3 c_{PDR}} + t_e . \quad \text{(B8)}$$

This paper has been typeset from a TEX/LATEX file prepared by the author.